SCIENTIFIC REPORTS
nature research

Check for updates

OPEN

Impact of strain, pressure, and electron correlation on magnetism and crystal structure of Mn_2GaC from first-principles

Martin Dahlqvist✉ & Johanna Rosen✉

The atomically laminated Mn_2GaC has previously been synthesized as a heteroepitaxial thin film and found to be magnetic with structural changes linked to the magnetic anisotropy. Related theoretical studies only considered bulk conditions and thus neglected the influence from possible strain linked to the choice of substrate. Here we employ first principles calculations considering different exchange–correlation functionals (PBE, PW91, PBEsol, AM05, LDA) and effect from use of + U methods (or not) combined with a magnetic ground-state search using Heisenberg Monte Carlo simulations, to study influence from biaxial in-plane strain and external pressure on the magnetic and crystal structure of Mn_2GaC. We find that PBE and PBE + U, with $U_{eff} \leq 0.25$ eV, gives both structural and magnetic properties in quantitative agreement with available experimental data. Our results also indicate that strain related to choice of substrate or applied pressure is a route for accessing different spin configurations, including a ferromagnetic state. Moreover, the easy axis is parallel to the atomic planes and the magnetocrystalline anisotropy energy can be increased through strain engineering by expanding the in-plane lattice parameter *a*. Altogether, we show that a quantitative description of the structural and magnetic properties of Mn_2GaC is possible using PBE, which opens the way for further computational studies of these and related materials.

In the 1960s, Nowotny and coworkers[1,2] discovered a family of inherently atomically laminated materials, which decades later were coined MAX phases. It is a ternary phase with the general formula $M_{n+1}AX_n$ ($n = 1–3$) where M is a transition metal (e.g. M = Ti, Cr, Mo, Zr), A is typically a group 13 to 16 element (e.g. A = Al, Si, Ga, Ge), and X is carbon or nitrogen. The material family, however, did not receive much attention until the mid-1990s and early 2000s when Ti_3SiC_2[3] and Ti_4AlN_3[4,5], respectively, was demonstrated to possess a unique combination of metallic and ceramic characteristics. Since then, MAX phases have been synthesized both as bulk material and in thin film form, and have been shown to exhibit extraordinary physical, chemical, electrical and mechanical properties[6]. Due to this, the MAX phases are being considered for protective coatings, electrical contacts, sensors, and high-temperature structural applications. They are also used as precursors for MXenes, their two-dimensional (2D) counterparts exhibiting extraordinary properties and are considered for a host of different applications[7–9].

The first experimental evidence of magnetic MAX phases were quaternary Mn-doped Cr_2GeC[10–12], Cr_2GaC[13–17] and Cr_2AlC[14,18,19] followed by $(Mo,Mn)_2GaC$[20,21] and $(V,Mn)_3GaC_2$[22]. Examples of ternary MAX phases with demonstrated magnetic properties are Cr_2AlC[23,24], Cr_2GeC[11,24], Cr_2GaC[13,25], Cr_2GaN[25], and Mn_2GaC[26–29]. The Cr-based phases have all been made in bulk form and as thin films, whereas Mn_2GaC have been synthesized in thin film form only. Potential applications of magnetic MAX phases range from spintronics to refrigeration, even though the research efforts have so far been focused solely on the discovery of new magnetic phases and compositions, and fundamentals of magnetic properties as summarized in Ref.[30].

It has previously been shown that Mn_2GaC simultaneously undergoes a magnetic and structural transition between 230 and 250 K[27]. With decreased temperature, the out-of-plane c axis contracts by 0.2% with an asymmetric change of the crystal structure as demonstrated from both X-ray diffraction[27] and neutron diffraction[28]. It has also been shown that at 214 K Mn_2GaC undergoes a first order magnetic phase transition from antiferromagnetic (AFM) at higher temperature to a non-collinear AFM spin structure with a large uniaxial

Thin Film Physics, Department of Physics, Chemistry and Biology (IFM), Linköping University, 581 83 Linköping, Sweden. ✉email: martin.dahlqvist@liu.se; johanna.rosen@liu.se

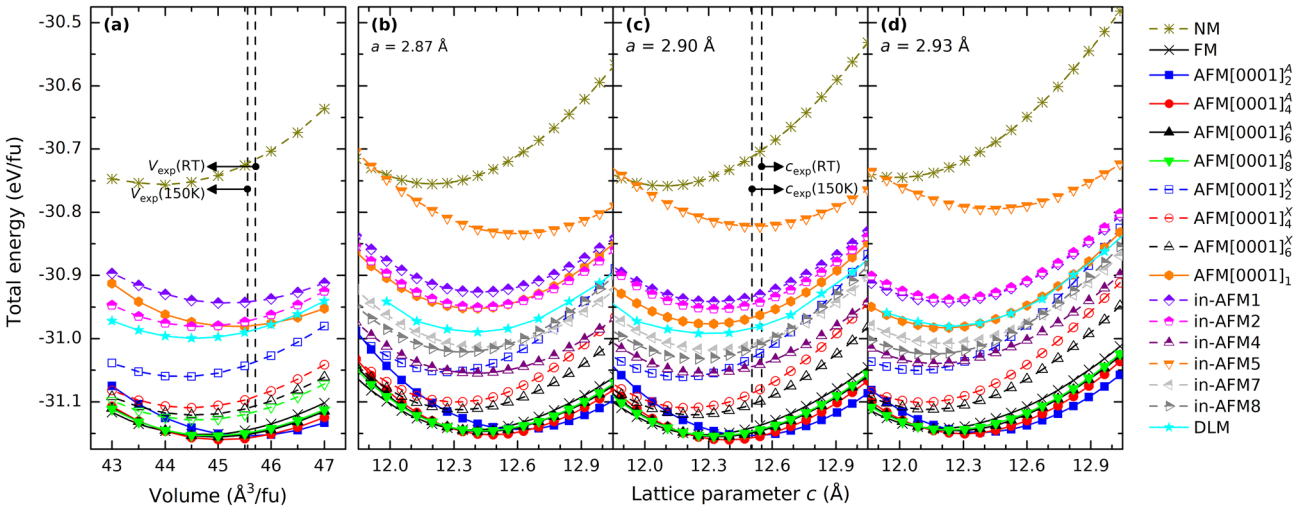

Figure 1. Total energy as a function of **(a)** volume and out-of-plane lattice parameter *c* for in-plane lattice parameter *a* being **(b)** 2.87 Å, **(c)** 2.90 Å, and **(d)** 2.93 Å assuming different spin configurations. All data presented are based on first-principles calculations employing the PBE exchange–correlation functional. The experimentally measured volume and lattice parameter *c* at room temperature (RT) and 150 K is represented by the vertical dashed line[26,27].

c-axis magnetostriction of 450 ppm[29]. Moreover, Mn_2GaC exhibits neutron-diffraction peaks consistent with long-range AFM order with a periodicity of two structural unit cells[28]. Also, a local magnetic moment of ~ 1.7 μ_B per Mn atom at 3 K and 5 T have been measured[27]. Based on supercell calculations, the magnetic critical order–disorder temperature T_c has been predicted to be 660 ± 133K[31]. Subsequent measurement found a Néel temperature of 507 K, at which Mn_2GaC changes from a (suggested) collinear AFM state to the paramagnetic (PM) state[29].

The need for using DFT + U methods for studying magnetic MAX phases have been debated, see Ref. [30] for further details. The first studies motivate the use of + U to get a better correlation between measured and calculated bulk modulus for Cr_2AC (A = Al, Ga, Ge)[32–37]. We have later shown that a better match can be achieved without any + U but through extended unit cells to describe non-trivial magnetic configurations[38,39]. Most investigations using + U for studying magnetic MAX phases use U from 0 to 2 eV, while, e.g., the hypothetical 2D Mn_2C MXene was studied using U = 4 eV and J = 1 eV, motivated by studies of Mn-based 3D compounds such as La(Mn,Zn)AsO, (Ga,Mn)N[40].

For the comparatively unexplored (theoretically and experimentally) Mn_2GaC phase, it is therefore motivated to investigate if the use of the ordinary generalized gradient approximation (GGA) is enough to describe the electron correlation, or if other functionals or DFT + U methods are necessary to describe the material. To address these questions, we here chose to investigate the structure and magnetic characteristics of Mn_2GaC under thin film constraints from choice of substrate, by applying tensile and compressive strain, both in- and out-of-plane, while considering different exchange–correlation functionals as well as use of DFT + U methods. In addition, we explore the easy axis and elaborate on its correlation to applied strain.

Result and discussion

In previous work of Mn_2GaC, we presented theoretical results valid for bulk synthesis conditions and thermodynamic equilibrium, by energies and volumes for various spin configurations obtained through complete relaxation of the unit cell volume, lattice parameters and atomic positions using the PBE functional[26–28,31]. Thin films, on the other hand, are known to realize also metastable states, sometimes far from thermodynamic equilibrium, with the lattice parameter of the film material influenced by the choice of substrate. Since Mn_2GaC has been synthesized as epitaxial thin films only, we here use the approach of performing structural relaxation under constraints that mimic thin film conditions. Depending on the substrate used, different lattice parameters may be achieved due to strain, which in turn may influence the magnetic properties.

As a first step, we include collinear spin configurations defined in Fig. 8 in Computational Details and in Table S1, using the PBE functional. We relax the structure (i) as function of volume and (ii) under the constraint of keeping the in-plane lattice parameter a fixed (at compressed (a = 2.87), equilibrium (a_0 = 2.90 Å), and tensile (a = 2.93 Å) strains) while changing the out-of-plane lattice parameter c. Figure 1 show the rather large spread in energy for the various spin configurations. For both volume relaxation and with Mn_2GaC constrained in-plane we find qualitatively similar results, with FM and AFM$[0001]^A_\alpha$ being lowest in energy. Optimized lattice parameters for considered collinear spin configurations are found in Table 1.

Based on Fig. 1 the focus will from this point forward be on magnetic spin configurations in the low-energy region and investigate how biaxial in-plane strain, i.e., effect from using different substrates, and pressure applied perpendicular to the film surface, i.e., along the surface normal (the *c*-axis), may alter the crystal structure and magnetic properties of Mn_2GaC. In addition, we also include a magnetic ground-state search at different biaxial

Magnetic state	Structural parameters			Local magnetic moments
	V (Å^3/fu)	a (Å)	c (Å)	|m| (μ_B/Mn atom)
NM	43.90	2.892	12.13	–
FM	44.72	2.899	12.29	1.95
AFM$[0001]_2^A$	45.57	2.903	12.48	2.26
AFM$[0001]_4^A$	45.07	2.898	12.39	1.99, 2.17
AFM$[0001]_6^A$	44.96	2.900	12.34	1.92, 2.01, 2.17
AFM$[0001]_8^A$	44.89	2.902	12.31	1.94, 1.97, 2.00, 2.16
AFM$[0001]_2^X$	44.29	2.898	12.18	1.59
AFM$[0001]_4^X$	44.46	2.900	12.21	1.52, 1.95
AFM$[0001]_6^X$	44.55	2.899	12.24	1.54, 1.91, 1.97
AFM$[0001]_8^X$	44.60	2.899	12.26	1.54, 1.94, 1.96, 1.97
AFM$[0001]_1$	45.31	2.925	12.23	1.83
In-AFM1	45.15	2.916	12.27	1.95
In-AFM2	44.67	2.892	12.35	1.99
In-AFM4	44.68	2.890	12.35	1.83, 1.95
In-AFM5	44.77	2.869	12.58	1.88
In-AFM7	44.79	2.895	12.34	1.79, 1.88, 2.05
In-AFM8	44.63	2.900	12.24	1.63, 1.86
DLM	44.67	2.887	12.38	0.57 to 2.27
Exp.[a]	45.70	2.90	12.55	Not reported
Exp.[b]	45.56	2.90	12.51	1.7 (at 3 K and 5 T)

Table 1. Calculated equilibrium volume V, lattice parameters a and c, and absolute magnetic moment per Mn atom for considered magnetic spin configurations of Mn_2GaC using the PBE exchange–correlation functional. Experimental results are included for comparison. [a]Structural parameters measured at room temperature[26]. [b]Structural parameters measured at 150 K[27].

strains and look at the magnetic anisotropy energies. Moreover, we herein also evaluate the effect from choice of different exchange correlation functionals.

Biaxial in-plane strain. We first investigate the impact from biaxial in-plane strain on the magnetic and the crystal structure of Mn_2GaC using PBE, PW91, PBEsol, AM05, and LDA functionals. We consider seven representative spin configurations (FM, AFM$[0001]_2^A$, AFM$[0001]_4^A$, AFM$[0001]_1$, AFM$[0001]_2^X$, AFM$[0001]_4^X$, and in-AFM2) along with the non-magnetic (NM) solution, at various strains. Independent of strain or functional used we find that the overall low-energy spin configurations are FM, AFM$[0001]_2^A$, and AFM$[0001]_4^A$, as shown in Fig. S1. These three spin configurations are therefore chosen for further evaluation.

In Fig. 2 the energy difference ΔE relative to a FM state, with $a_0 = 2.90$ Å, and local magnetic moments as function of biaxial in-plane strain is shown for FM, AFM$[0001]_2^A$, and AFM$[0001]_4^A$. Looking at ΔE in the top panels in Fig. 2, four functionals, PW91, LDA, PBEsol, and AM05, show the same spin configuration order with FM lowest in energy, AFM$[0001]_2^A$ highest in energy, and AFM$[0001]_4^A$ in-between. For PBE, AFM$[0001]_4^A$ is lowest in energy at compressive strains and up to + 1% tensile strain. Above + 1.3%, AFM$[0001]_2^A$ is found to be of lowest energy. Only two functionals, PBE and PW91, results in an energy minimum at or close the reported experimental value of $a = 2.90$ Å. LDA, PBEsol, and AM05 all overbind with a minimum ΔE at compressive strains below − 1.5%.

From a structural point of view, we find a decrease in lattice parameter c with increasing a, see the mid panels in Fig. 2. For all functionals we find c to be smallest for FM and largest for AFM$[0001]_2^A$. The reported value of c (12.55 Å) for synthesized Mn_2GaC, with $a = 2.90$ Å, is indicated by the dashed horizontal line. Both PBE and PW91 give c values close to reported, while overbinding (resulting in too small c) is large for PBEsol, AM05, and especially LDA.

Calculated local moments, bottom panels of Fig. 2, are in general highest for AFM$[0001]_2^A$ and lowest for FM. For AFM$[0001]_4^A$ we observe two different values which can be related to its spin structure that on a local scale resembles both FM and AFM$[0001]_2^A$. This can be seen by comparing the magnetic structures in Fig. 7d with Fig. 6a, c in Computational Details, where the lower value corresponds to a FM surrounding, with Mn atoms of parallel spins across the Ga layer, while those of higher value resemble AFM$[0001]_2^A$, with Mn atoms of antiparallel spins across the Ga layer.

The internal crystal structure of Mn_2GaC can be described by two different Mn–Mn interlayer distances illustrated in Fig. 8q in Computational Details; (i) d_X which represents the distance between two Mn layers interleaved with carbon, or X in general, and (ii) d_A which represents the distance between two Mn layers interleaved with Ga, or A in general. Fig. S2 show interlayer distances d_X and d_A as function of biaxial in-plane strain. For AFM$[0001]_4^A$ there are two different d_A values which can be related to the difference in the spin

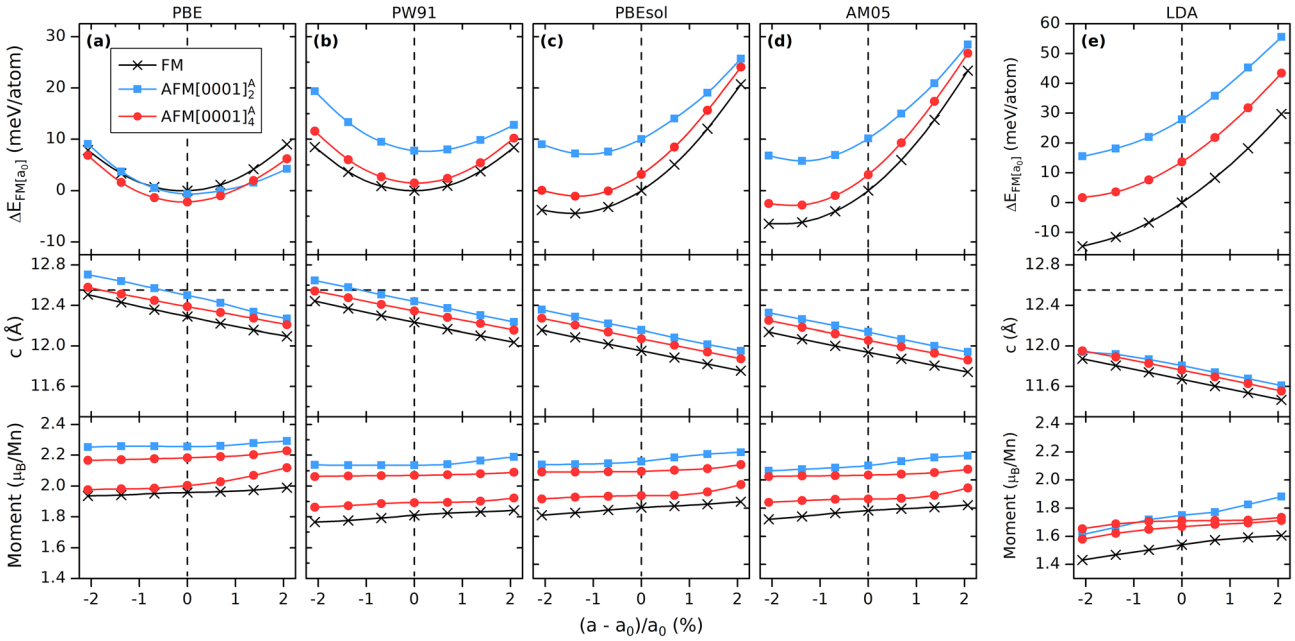

Figure 2. Energy relative to the FM state with $a_0 = 2.90$ Å (upper panels), lattice parameter c (mid panels), and local magnetic moment (bottom panels) as function of biaxial in-plane strain for FM, AFM[0001]$^{A}_{2}$, and AFM[0001]$^{A}_{4}$ spin configurations using **(a)** PBE, **(b)** PW91, **(c)** PBEsol, **(d)** AM05, and **(e)** LDA exchange–correlation functionals. The experimentally measured lattice parameter *a* of 2.90 Å is represented by the vertical dashed line and *c* of 12.55 Å is represented by the horizontal dashed line in the mid panels[26,27].

configuration close to the Mn layer. Similar to the two different magnetic moments in Fig. 2. The lower d_A value is similar to those found for FM, as are their local moments, while the larger d_A value is close to those obtained for AFM[0001]$^{A}_{2}$. For d_X, only one set of values is found for each of the three spin configurations, and these configurations are, on a local scale, equivalent.

Based on the large tendencies for overbinding when using PBEsol, AM05, and LDA functionals, we chose to investigate impact from biaxial strain upon addition of + U, using the approach by Dudarev[41]. It should be noted that in a theoretical study of the hypothetical 2D Mn_2C MXene[40], which is the 2D counterpart of Mn_2GaC after removal of Ga, $U = 4$ eV and $J = 1$ eV was used. Such value of U can not directly be extrapolated to also be valid for the 3D Mn_2GaC. We have therefore used several values for U_{eff}, though for the results presented herein, U_{eff} is chosen based on an identified minimum ΔE close to $a_0 = 2.90$ Å and values for *c* close to the reported value of 12.55 Å. A moderate value of $U_{eff} = 1$ eV is chosen for PBE and PW91 as their numbers are already close to or slightly larger than reported experimental values[26,27]. Both PBEsol and AM05 require $U_{eff} = 2.5$ eV, while for LDA a value of $U_{eff} = 4$ eV is needed. To ensure that no other spin configurations than FM, AFM[0001]$^{A}_{2}$, and AFM[0001]$^{A}_{4}$ may be a relevant low-energy solution, we also consider AFM[0001]$_1$, AFM[0001]$^{X}_{2}$, AFM[0001]$^{X}_{4}$, in-AFM2, and NM. As shown in Fig. S3, the low-energy spin configurations are those with parallel spins within each Mn-C-Mn trilayer, i.e., FM, AFM[0001]$^{A}_{2}$, and AFM[0001]$^{A}_{4}$. Interesting to note is that for all six functionals we find the order of the spin configurations to be the same, with AFM[0001]$^{A}_{2}$ lowest in energy followed by AFM[0001]$^{A}_{4}$ and FM as seen in Fig. 3. Moreover, for AFM[0001]$^{A}_{4}$ in Fig. 3 and Fig. S4 there is no longer two distinct values of neither the local magnetic moment or d_A, as compared to Fig. 2 and Fig. S4, when + U is not considered. Instead, these values are similar to values found for both FM and AFM[0001]$^{A}_{2}$.

The results presented for Mn_2GaC at biaxial strain shows that PBEsol, AM05, and LDA all overbind and with FM as the lowest energy spin configuration. PBE and PW91, on the other hand, results in an energy minimum at or close the reported experimental value of $a = 2.90$ Å and with magnetic moments slightly overestimated than experimentally reported[27]. The use of + U, with U_{eff} values chosen in such a way to mimic experimentally reported lattice parameters, results in local magnetic moments much larger than those reported experimentally[27]. We also note, independent of functional or if using + U or not, that the corresponding low-energy spin configurations always corresponds to those with FM ordering within Mn-C-Mn trilayer, i.e., FM and AFM[0001]$^{A}_{\alpha}$ (α = 2 and 4). Such FM ordering within Mn-C-Mn trilayer has previously been experimentally demonstrated for quaternary MAX phases $(Cr_{0.5}Mn_{0.5})_2GaC$[15,16] and $(Mo_{0.5}Mn_{0.5})_2GaC$[20,21] using ferromagnetic resonance (FMR) measurements. We thus conclude that using PBE, without + U or a with a small U_{eff}, gives crystallographic structures, including the asymmetric structural changes during the magnetic transition around 250 K and below[27], and magnetic structures comparable to those found from vibrating sampling magnetometry, X-ray and neutron diffraction [26–28]. Note that the use of no U or a small value of U_{eff} for 3D Mn_2GaC, as compared to $U = 4$ eV and $J = 1$ eV used for 2D Mn_2C[40], could be related to the interference by the Ga layer, imposing periodic screening of the Mn-C-Mn trilayers.

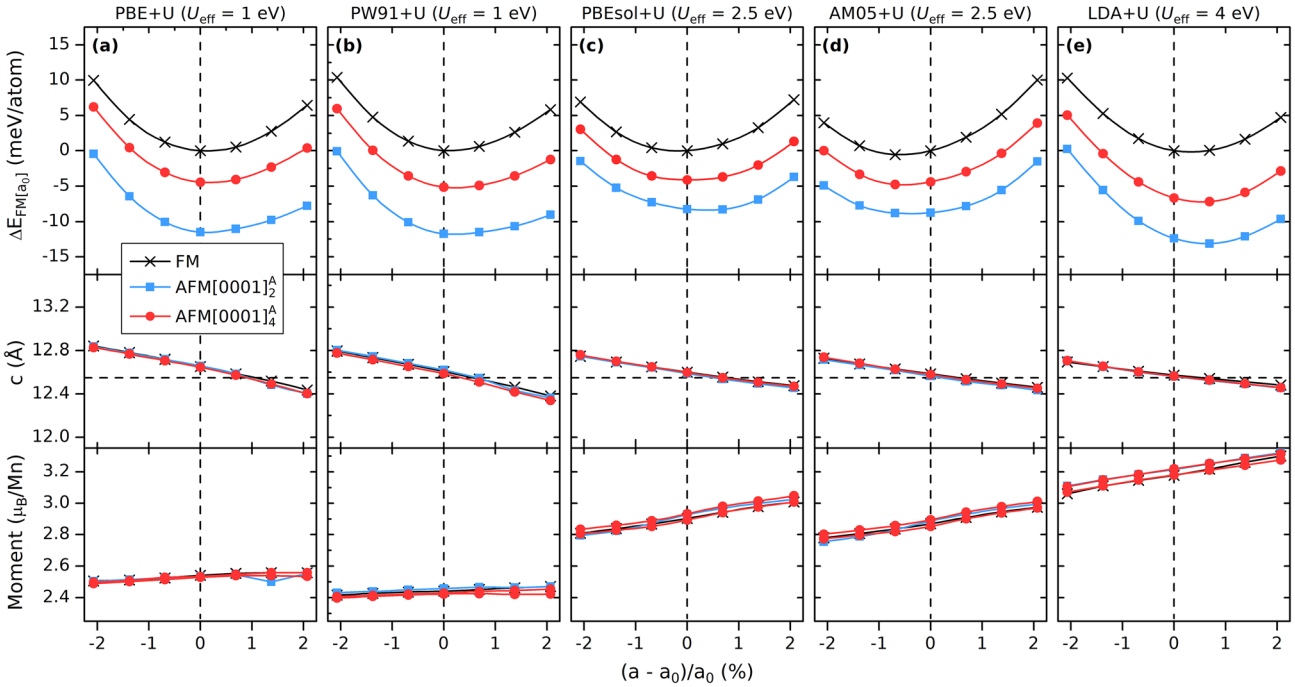

Figure 3. Energy relative ferromagnetic solution with $a_0 = 2.90$ Å, ΔE (top panels), and local magnetic moment (bottom panels) as function of strain for FM, AFM$[0001]^A_2$, and AFM$[0001]^A_4$ spin configurations using **(a)** PBE + U, **(b)** PW91 + U, **(c)** PBEsol + U, **(d)** AM05 + U, and **(e)** LDA + U exchange–correlation functionals. Considered U_{eff} values are given at the top of each panel. The experimentally measured lattice parameter a of 2.90 Å is represented by the vertical dashed line and c of 12.55 Å is represented by the horizontal dashed line in the mid panels[26,27].

Magnetic ground-state search at biaxial in-plane strain. To this point, only collinear spin configurations have been considered. From analysis of magnetic measurements of Mn_2GaC there are indications that the magnetic structure is, or at least bears strong resemblance to, AFM $[0001]^A_4$. One approach to identify or get inspiration for other possible and more complex noncollinear spin configurations is to perform a representative magnetic ground-state search. In Ref.[27] such a search was performed and several magnetic spin configuration close to degenerate in energy was found as a function of volume.

Motivated by the thin films of Mn_2GaC synthesized to date, a representative magnetic ground-state search needs to keep a static to mimic thin film conditions for different substrates. We used the same approach as in Ref.[27] and performed a magnetic ground-state search using a coarse-grained super-moment representation, depicted in Fig. 9 in Computational Details, aiming to find additional magnetic spin configurations. To preserve control of the crystal structure, and the corresponding energies, we made the following approximations;

(i) a and interlayer distance d_X were kept fixed while varying the interlayer distance d_A.
(ii) we only considered low-energy candidates with parallel spins within the Mn-C-Mn trilayer, i.e., FM, AFM$[0001]^A_2$, AFM$[0001]^A_4$, AFM$[0001]^A_6$ and AFM$[0001]^A_8$.
(iii) we used the PBE exchange–correlation functional with no + U.

Based on these constraints we calculated the total energies, shown in Fig. S5, and used these along with the Connolly-Williams structure inversion method[42,43] to derive the exchange interactions J_{ij}'s for the first four super-moment interlayer coordination shells, see Fig. S6. In order to find possible long-range magnetic spin configurations, we considered supermoment chains with up to 40 beads. This range also ensures that we minimize effects related to size and boundary conditions. The energy dependence of the number of beads included in the chain at various values of d_A is shown in Fig. S8. From this point forward, we only present the low-energy solutions for each set of a, d_X, and d_A, independent on the number of beads used.

Figure 4 summarizes the result from our Heisenberg Monte Carlo simulations. Figure 4a shows a schematic illustration of the two individual angles defining the spin-orientation between nearest and next nearest neighbour supermoment spin vectors, θ_1 and θ_2. Details of θ_1 and θ_2 extracted from low-energy solutions when varying a, d_X, and d_A is shown in Fig. S8. A selection of representative low-energy solutions is illustrated in Fig. 4b along with related information such as interlayer distance d_A, corresponding lattice parameter c, and average and/or individual angle between nearest and next nearest neighbour supermoment spin vectors, θ_1 and θ_2. Note that for $d_A = 4.058$ Å ($c = 12.30$ Å), two different solutions were found with equal energy, III and IV, each with two distinct values of θ_1, as given within parenthesis, though with an average value of 90°. Similar results are found when Mn_2GaC is under compressive (-1%, $a = 2.87$ Å) and tensile (+1%, $a = 2.93$ Å) strain, shown in Fig. S8,

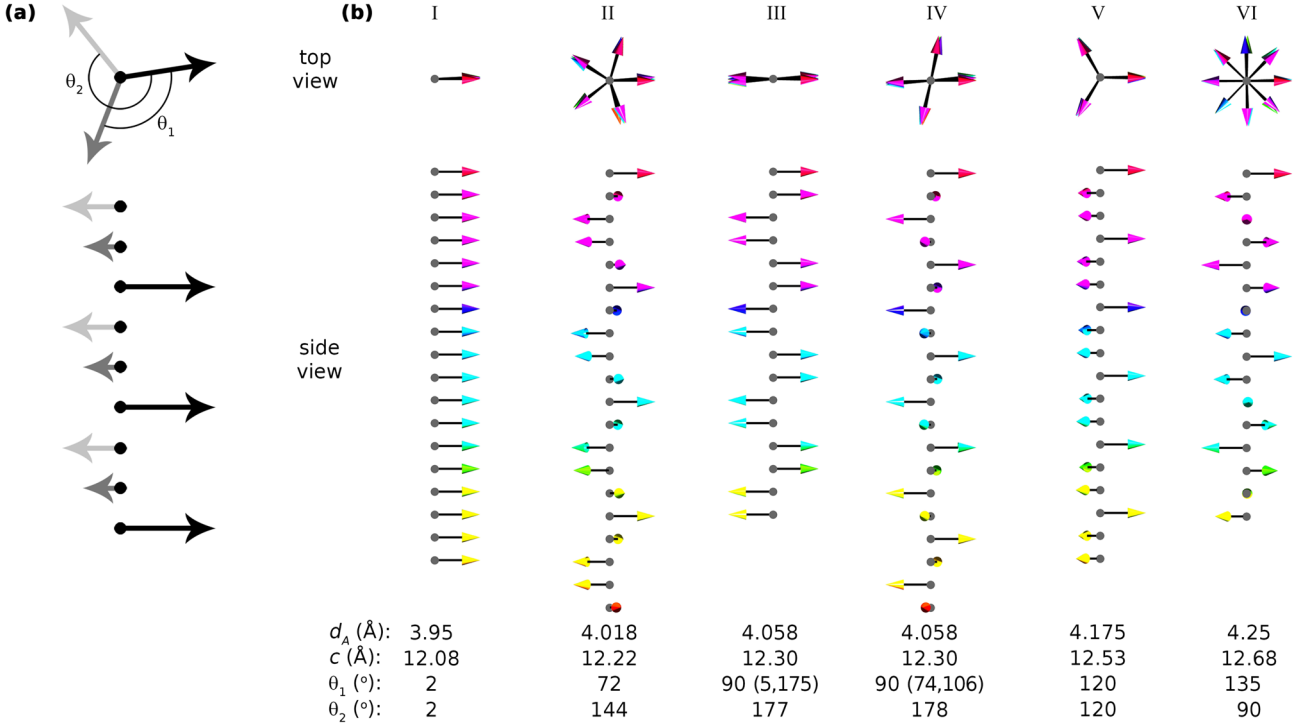

Figure 4. **(a)** Schematic illustration individual angles defining the spin-orientation between nearest and next nearest neighbour supermoment spin vectors, θ_1 and θ_2. **(b)** Selected low-energy spin configurations extracted from the Heisenberg Monte Carlo simulations at various d_A where $a = 2.90$ Å and $d_X = 2.09$ Å.

although shifted to larger and smaller d_A, respectively. When smaller(larger) values of d_X are considered, the results are shifted to larger(smaller) value of d_A, shown in Fig. S8.

Inspired by the obtained noncollinear spin spiral configurations depicted in Fig. 4b, we considered a small set of representative configurations for evaluation using first-principles calculations. For $a_0 = 2.90$ Å, we use PBE + U with U_{eff} from 0 to 2 eV and compare energies, structural parameters and magnetic moments, see Fig. 5. The calculated energies relative to the FM state is shown in in Fig. 5a. With ordinary PBE ($U_{\text{eff}} = 0$ eV), the considered noncollinear spin configurations are all in between FM and the lowest energy AFM$[0001]_4^{\text{A}}$. For PBE + U, with increasing U_{eff} up to 0.5 eV, all AFM configurations, collinear and noncollinear, decreases in energy relative to FM.

Measured lattice parameter c at room temperature (RT) and at 150 K, indicated by horizontal lines in Fig. 5b, clearly shows that using ordinary PBE gives too small c while $U_{\text{eff}} \geq 0.5$ eV gives too large values of c. Moreover, not only does c, the interlayer distance d_A and the local magnetic moment increase with increasing U_{eff}, but we also find that they merge towards similar values independent of considered spin configuration. This is most clear for $U_{\text{eff}} \geq 1$ eV. This is indicative of a parameter forcing the magnetic moment to be localized, raising a question of the proper value of U_{eff} to describe Mn_2GaC in particular and magnetic MAX phases in general. These results indicate the PBE or PBE + U (with $U_{\text{eff}} \leq 0.25$ eV) is the most appropriate functionals to use until proven otherwise for describing Mn_2GaC when compared to experimental results[26–29].

Mn_2GaC under pressure. Here we investigate how the magnetic properties and crystal structure of Mn_2GaC can be altered when pressure is applied perpendicular to the film surface, i.e., along the surface normal (the c-axis). We only consider low energy spin configurations FM, AFM$[0001]_2^{\text{A}}$, and AFM$[0001]_4^{\text{A}}$, and choose to not include noncollinear spin configurations since the energies for these are all found in between those of FM, AFM$[0001]_2^{\text{A}}$ and AFM$[0001]_4^{\text{A}}$. Starting with the thermodynamic stability of Mn_2GaC, the possibility of phase transition between considered spin configurations is investigated. The enthalpies are calculated according to

$$H[p] = E[p] + pV[p], \tag{1}$$

where $E[p]$ and $V[p]$ is the equilibrium energy and volume, respectively, at given pressure p.

Figure 6a depicts the pressure vs U_{eff} where the color represents the spin configuration of lowest enthalpy for $a_0 = 2.90$ Å. For ordinary PBE ($U_{\text{eff}} = 0$) we find that at 3.8 GPa there is a transition from AFM$[0001]_4^{\text{A}}$ to FM. When U_{eff} increases AFM$[0001]_2^{\text{A}}$ becomes the favoured configuration at small applied pressures. FM is still accessible for $U_{\text{eff}} > 0$ but an increased pressure is required.

To explore potential pathways for attaining a FM state, we also probe for lowest enthalpy spin configuration on a pressure vs biaxial-in-plane strain grid for a range of lattice parameter a, from compressive ($a = 2.86$ Å, − 2.07%) to tensile ($a = 2.94$ Å, + 2.07%) strain. The various values of a thus represent substrates of different size. Figure 6b depicts pressure vs bi-axial in-plane strain for ordinary PBE ($U_{\text{eff}} = 0$ eV) where the color represents

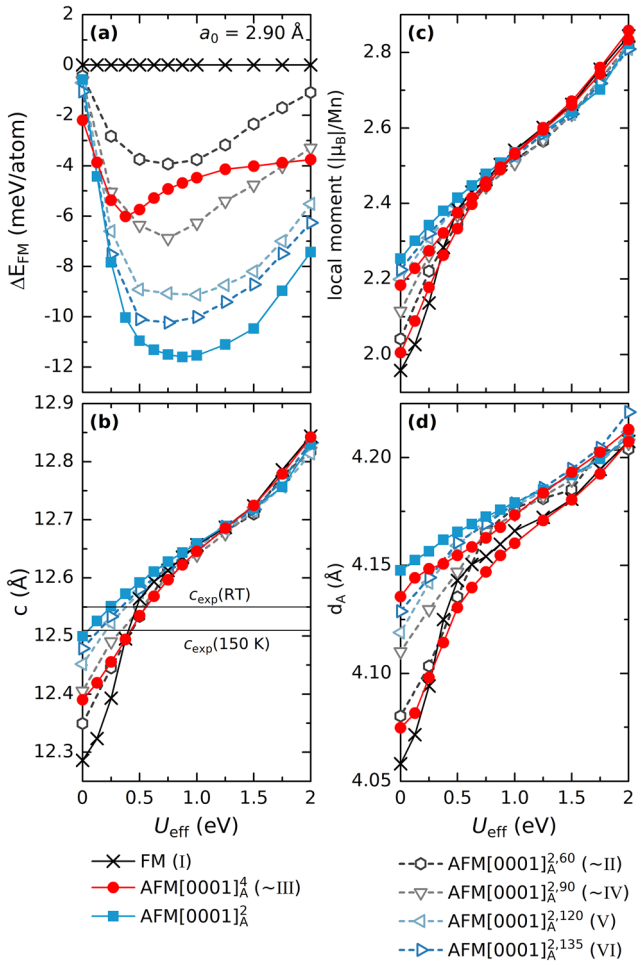

Figure 5. **(a)** Energy relative to the FM state, **(b)** lattice parameter *c*, **(c)** local magnetic moment, and **(d)** interlayer distances d_A for Mn_2GaC, with $a_0 = 2.90$, Å as function U_{eff} for collinear FM, AFM[0001]$^A_2$, and AFM[0001]$^A_4$ and noncollinerar AFM[0001]$^{A,60}_2$, AFM[0001]$^{A,90}_2$, AFM[0001]$^{A,120}_2$, and AFM[0001]$^{A,135}_2$ spin configurations using the PBE + U exchange–correlation functional.

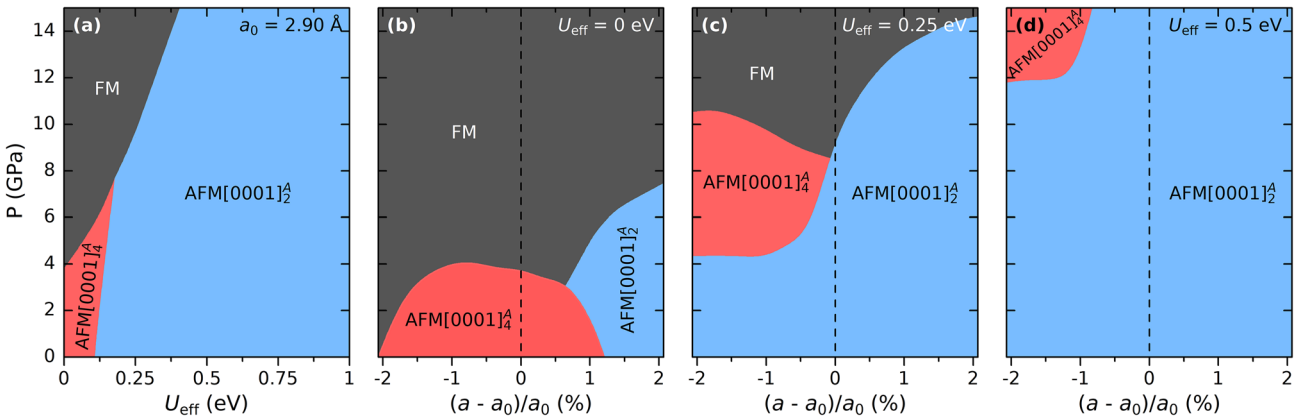

Figure 6. Spin configuration of lowest enthalpy for **(a)** a pressure vs U_{eff} grid, and for a pressure vs biaxial-in-plane strain grid for U_{eff} equal to **(b)** 0 eV, **(c)** 0.25 eV, and **(d)** 0.5 eV, using the PBE + U exchange–correlation functional.

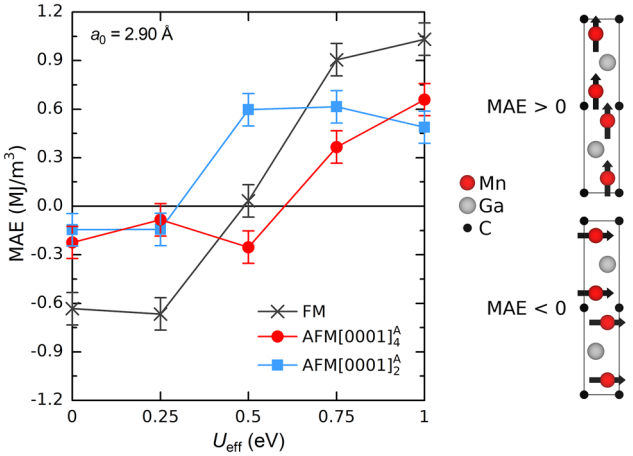

Figure 7. Magnetic anisotropy energy (MAE) as a function U_{eff} when considering FM, AFM$[0001]^A_4$, and AFM$[0001]^A_2$ spin configurations and using the PBE + U exchange–correlation functional. The estimated error bar from k-point convergence is 0.1 MJ/m^3. The schematic shows the preferential spin alignment dependent on sign of the MAE.

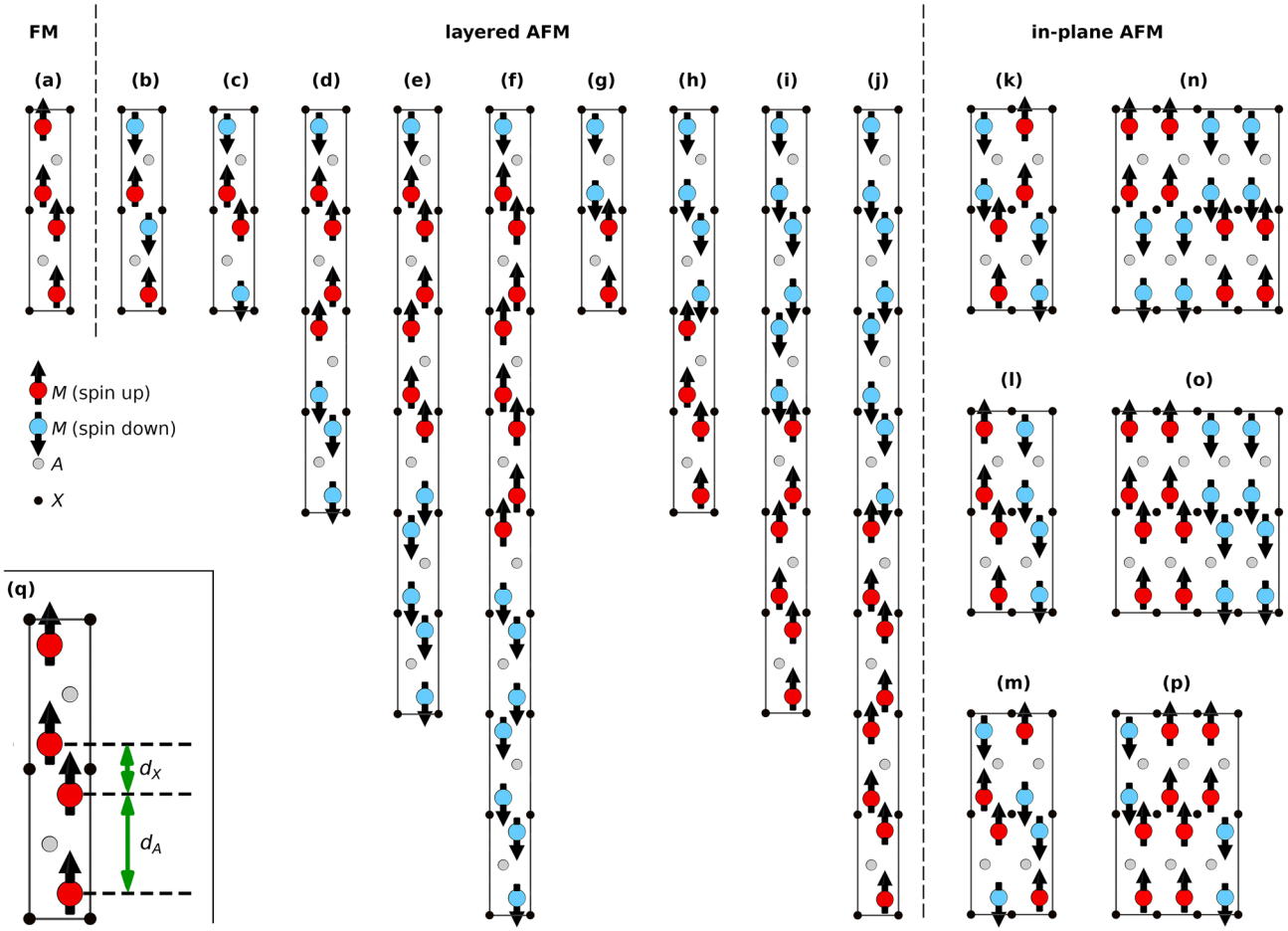

Figure 8. Schematic representation of collinear spin configurations for a M_2AX phase where **(a)** represents FM, **(b)** AFM$[0001]_1$, **(c)** AFM$[0001]^A_2$, **(d)** AFM$[0001]^A_4$, **(e)** AFM$[0001]^A_6$, **(f)** AFM$[0001]^A_8$, **(g)** AFM$[0001]^X_2$, **(h)** AFM$[0001]^X_4$, **(i)** AFM$[0001]^X_6$, **(j)** AFM$[0001]^X_8$, **(k)** in-AFM1, **(l)** in-AFM2, **(m)** in-AFM3, **(n)** in-AFM4, **(o)** in-AFM5, and **(p)** in-AFM6. **(q)** The interlayer distances d_X and d_A is indicated. Projections are viewed along the $[1-210]$ direction.

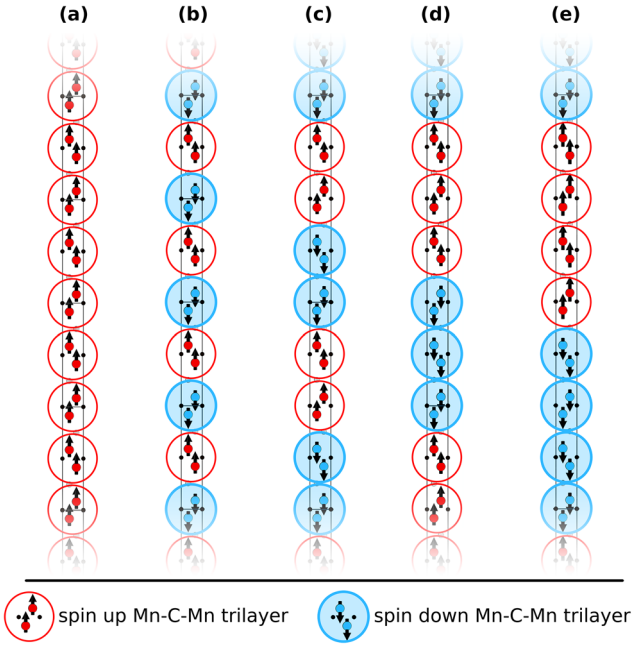

Figure 9. Schematic illustration of the coarse-grained super-moment model where each Mn-C-Mn trilayer is represented by a super-moment bead, red for spin up and blue for spin down, in Mn_2GaC for **(a)** FM, **(b)** AFM$[0001]_2^A$, **(c)** AFM$[0001]_4^A$, **(d)** AFM$[0001]_6^A$, and **(e)** AFM$[0001]_8^A$ spin configurations.

the spin configuration of lowest enthalpy. At zero pressure and from compressive up to 1.25% tensile biaxial strain, we find AFM$[0001]_4^A$, while further increase in tensile strain results in a transition to AFM$[0001]_2^A$. When pressure is applied, the enthalpy difference between AFM$[0001]_\alpha^A$ and FM decreases. For $a_0 = 2.90$ Å (0%) we find that at 3.8 GPa there is a transition from AFM$[0001]_4^A$ to FM. This transition is associated with a corresponding decrease in c, magnetic moment, and interlayer distances d_A and d_X, see details in Fig. S9, and is found at both compressive (down to -2%) and tensile (up to + 1.25%) biaxial strain for an applied pressure up to 4 GPa. Between tensile strain from + 0.75 to 1.25% there is a transition from AFM$[0001]_4^A$ to AFM$[0001]_2^A$ with increasing pressure before accessing FM. Furthermore, for a tensile biaxial strain above + 1.25% and at zero or low pressure we find AFM$[0001]_2^A$. When pressure is applied there is a transition from AFM$[0001]_2^A$ to FM, though shifted to higher pressure for an increased tensile strain.

For $U_{eff} \geq 0.25$ eV, see Fig. 6c, d, we find similar magnetic transitions as for ordinary PBE, but shifted towards more compressive strain and higher pressure. AFM$[0001]_2^A$ is the favoured spin configuration at low pressure. Focusing on $U_{eff} = 0.25$ eV at $a_0 = 2.90$ Å (0%), we find that at 9.1 GPa there is a transition from AFM$[0001]_2^A$ to FM associated with a significant change in both magnetic moment and crystal structure, shown in Fig. 5b, c, as compared to a AFM$[0001]_4^A$ to FM transition.

These results thus indicate that through manipulation of the strain within the thin film plane, e.g., through the choice of substrate, it is possible to strain-engineer accessible spin configurations. Moreover, through exertion of an external force, e.g., by applying a rather moderate pressure perpendicular to the film plane, one would enable a magnetic transition from AFM to FM. The significant change both in terms of crystal and magnetic structure during this transition should allow experimental verification.

Magnetocrystalline anisotropy energy. There are so far no studies reported on the magnetocrystalline anisotropic energy (MAE) for Mn_2GaC, neither experimental nor theoretical. Measurements on a related phase where 50% Mn in Mn_2GaC is substituted for Mo in $(Mo_{0.5}Mn_{0.5})_2GaC$ shows that the easy axis is in-plane, despite having a small MAE of 4.5 ± 0.3 kJ/m^3 at 100 K favoring an out-of-plane orientation [21]. Vibrating sampling magnetometry (VSM) measurements on Mn_2GaC demonstrates that spins are aligned within the Mn planes[26,27]. We chose to investigate the MAE for Mn_2GaC by including the spin–orbit coupling and by using the PBE + U exchange–correlation functional for $0 \leq U_{eff} \leq 1$ eV. Based on results presented in previous sections of this work and in related experimental results[26–28], we only consider the three low-energy collinear spin configurations, i.e., FM, AFM$[0001]_2^A$, and AFM$[0001]_4^A$.

The MAE in Fig. 7 was calculated as the energy difference between the configurations with spins aligned in-plane, i.e. parallel to the Mn layer, and normal to the Mn layers, MAE = E(→) − E(↑). To ensure convergence for calculated MAE we considered various k-point densities, see Fig. S11. From this we estimated an error of ± 0.1 MJ/m^3. The structures used are for $a_0 = 2.90$ Å and for each U_{eff} we used an optimized structure with c given Fig. 5b.

For $U_{eff} \leq 0.25$ eV, we find negative values for MAE which is indicative of preferential spin alignment within the Mn planes. Note that this is consistent with experimental reports[26,27]. At larger U_{eff}, MAE change sign and

for $U_{eff} \geq 0.75$ eV all spin configurations show preferential for out-of-plane spin alignment. Here we again notice how sensitive the results are with respect to value of U_{eff} and that results for $U_{eff} > 0.25$ are inconsistent with experiments. In addition, for ordinary PBE, we find a negative MAE for various a and c values, see Fig. S12, showing that FM and AFM$[0001]_4^A$ having spins aligned in-plane become energetically more favorable upon tensile in-plane and compressed out-of-plane strain. AFM$[0001]_2^A$, on the other hand, show a MAE value being almost constant for here considered lattice parameters.

Our results of having preferential spin alignment within the Mn planes, for $U_{eff} \leq 0.25$ eV, are consistent with VSM measurements on Mn_2GaC showing that spins are aligned within the Mn planes[26,27]. For AFM$[0001]_4^A$ and AFM$[0001]_2^A$ the calculated MAE for $U_{eff} \leq 0.25$ eV is in the range − 100 to − 300 kJ/m^3. We suggest that the MAE for a Mn_2GaC thin film could be increased by expanding the in-plane lattice parameter a and thus reducing the value of c to minimize the stress in the c direction, as exemplified in Fig. S12(c).

Conclusion

We here present a first principles study of the structural and magnetic properties of the atomically laminated Mn_2GaC, with emphasis on effect of biaxial in-plane strain, pressure, and choice of different exchange–correlation functionals, aiming towards a relevant description of the structural and magnetic properties attainable for Mn_2GaC in thin film form. Here we note that previous theoretical results were primarily relevant for bulk synthesis conditions, i.e. for an equilibrium volume and energy. It is found that use of the PBE functional or PBE + U ($U_{eff} \leq 0.25$ eV) gives both structural and magnetic properties in good quantitative agreement with available experimental data. PW91, PBEsol, AM05, and LDA functionals and/or use of an + U approach result in structures and magnetic characteristics not compatible with the same experimental reports. Through a magnetic ground-state search we find several noncollinear magnetic configurations which bears structural and magnetic resemblance to low-energy collinear candidates. Notable is that through strain-engineering by choice of substrate or applied pressure, different spin configurations may be accessible, which in turn suggest a tuning potential of the magnetic properties, including attaining a FM spin state. Furthermore, we also suggest that the easy axis in Mn_2GaC is parallel to the atomic planes and that the MAE can be increased through strain engineering by expanding the in-plane lattice parameter a, thus reducing the value of the out-of-plane lattice parameter c, which strengthen the spin orientation parallel to the atomic planes. Finally, the results presented here suggest that a quantitative description of the structural and magnetic properties of Mn_2GaC is possible using PBE, which opens the way for further computational studies of these and related materials.

Computational details. All first-principles density functional theory (DFT) calculations are performed using the projector augmented wave method[44,45] as implemented within the Vienna ab initio simulation package (VASP)[46–48], with a plane-wave energy cutoff of 400 eV. For sampling of the Brillouin zone we used the Monkhorst–Pack scheme[49]. Within this work we use different exchange–correlation functionals to study their dependence on structure and magnetic properties. If not stated otherwise, the generalized gradient approximation (GGA) as parameterized by Perdew-Burke-Ernzerhof (PBE)[50,51] has been used. In parts of the work we also used the PBE revised for solids (PBEsol)[52], the Perdew–Wang 91 (PW91)[53], and AM05[54–56] GGAs, and the local density approximation (LDA)[57] functionals. In addition, we also used the rotationally invariant approach as proposed by Dudarev[41]. Note that within this formalism the onsite Coulomb parameter U and the exchange parameter J are spherically averaged into a single effective interaction parameter $U_{eff} = U - J$ which does not depend on their individual values. The equilibrium structures are obtained by minimization of the total energy for an a and c lattice parameter grid with full relaxation of atomic positions until forces are converged below 10^{-4} eV Å^{-1}. Calculations including spin–orbit coupling (SOC) have been performed in the mode implemented in VASP by Hobbs et al.[58] and Marsman and Hafner[59], in a two-step procedure. First, we performed a scalar-relativistic calculation to obtain the correct geometry, followed by calculations including spin–orbit coupling with spins aligned along the c-axis, i.e. parallel/antiparallel to [0001] axis, and perpendicular to the c-axis, i.e. parallel/antiparallel to both [1–100] and [1–210] axis.

We have considered several collinear magnetic spin configurations for Mn_2GaC, most of them have been defined previously for a general M_2AX phase[27,38,39]. A schematic representation is shown in Fig. 8, and includes a ferromagnetic (FM), nine layered antiferromagnetic (AFM), and six in-plane AFM spin configurations. The notation used for layered AFM spin configurations is defined as follows; single layer AFM with spins changing sign for every M layer corresponds to AFM$[0001]_1$, and multilayered AFM ordering with α consecutive M layers (where α = 2, 4, 6, 8) of the same spin direction before changing sign upon crossing an A or an X layer corresponds to AFM$[0001]_\alpha^A$ and AFM$[0001]_\alpha^X$, respectively[27,38]. In addition, the paramagnetic (PM) have been modelled using the disorder local moment (DLM)[60] approach where the spin-correlation functions are equal to zero for at least the first 10 M-coordination shells. The disordered magnetic moments in $(Mn\uparrow_{0.5}Mn\downarrow_{0.5})_2GaC$ is simulated by means of the special quasi-random structure (SQS) method[61,62] using a supercell with 64 Mn, 32 Ga, and 32 C atoms, i.e., 4 × 4 × 1 or 16 M_2AX unit cells. A strict definition of these collinear spin configurations is given in Table S1 where the spin correlation function Φ_i is given for the first 10 M-shells.

For the magnetic ground-state search we used a coarse-grained model, shown in Fig. 9 in Computational Details, where the local moment of Mn atoms in a Mn-C-Mn trilayer plane is represented by a supermoment. This is motivated by all low-energy spin configurations of Mn_2GaC having parallel spin directions within their Mn-C-Mn trilayers. The supermoment model is thus described using only magnetic exchange interactions (MEI) across the A layer along the c axis and cannot be used to modelling critical temperature since the MEI within a Mn-C-Mn tri-layer is neglected, and hence the exact temperature from the Monte Carlo simulation becomes irrelevant as it scales with the area of each layer. The spin correlation function Φ_i for the five considered

spin configurations are given in Table S2. The essence of the approach is to identify possible non-trivial spin configurations through us of Monte Carlo simulations using a Heisenberg Hamiltonian.

$$\mathcal{H} = -\sum(i \neq j) J_{ij} \mathbf{e_i} \cdot \mathbf{e_j}, \tag{2}$$

where J_{ij} is the MEI between pairs of super-moments (i, j), with unit vectors $\mathbf{e}_i$ and $\mathbf{e}_j$ along the local magnetic moment at site i and j, represented by a chain of super-moments. The exchange interactions J_{ij}'s are derived for the first four super-moment interlayer coordination shells using the magnetic Connolly-Williams structure inversion method[42,43], shown in Table S2 in combination with energies from first-principles calculations. To avoid possible metastable solutions, we initially set the temperature to a large value, and then slow cooling towards 0 K and to allow long-range magnetic interactions we used supermoment chains including up to 40 beads.

Received: 5 November 2019; Accepted: 10 June 2020
Published online: 09 July 2020

References

1. Nowotny, H. Strukturchemie einiger Verbindungen der Übergangsmetalle mit den elementen C, Si, Ge, Sn. *Prog. Solid State Chem.* **5**, 27–70 (1971).
2. Nowotny, H., Rogl, P. & Schuster, J. C. Structural chemistry of complex carbides and related compounds. *J. Solid State Chem.* **44**, 126–133 (1982).
3. Barsoum, M. W. & El-Raghy, T. Synthesis and characterization of a remarkable ceramic: Ti_3SiC_2. *J. Am. Ceram. Soc.* **79**, 1953–1956 (1996).
4. Barsoum, M. W. The $M_{N+1}AX_N$ phases: A new class of solids; thermodynamically stable nanolaminates. *Prog. Solid State Chem.* **28**, 201–281 (2000).
5. Barsoum, M. W. & El-Raghy, T. The MAX phases: Unique new carbide and nitride materials—Ternary ceramics turn out to be surprisingly soft and machinable, yet also heat-tolerant, strong and lightweight. *Am Sci.* **89**, 334–343 (2001).
6. Barsoum, M. W. *MAX Phases, Properties of Machinable Ternary Carbides and Nitrides* (Wiley, New York, 2013).
7. Naguib, M. *et al.* Two-dimensional nanocrystals produced by exfoliation of Ti3AlC2. *Adv. Mater.* **23**, 4248–4253 (2011).
8. Naguib, M. *et al.* Two-dimensional transition metal carbides. *ACS Nano* **6**, 1322–1331 (2012).
9. Anasori, B., Lukatskaya, M. R. & Gogotsi, Y. 2D metal carbides and nitrides (MXenes) for energy storage. *Nat. Rev. Mater.* **2**, 16098 (2017).
10. Ingason, A. S. *et al.* Magnetic self-organized atomic laminate from first principles and thin film synthesis. *Phys. Rev. Lett.* **110**, 195502 (2013).
11. Liu, Z., Waki, T., Tabata, Y. & Nakamura, H. Mn-doping-induced itinerant-electron ferromagnetism in Cr_2GeC. *Phys. Rev. B* **89**, 054435 (2014).
12. Tao, Q. Z. *et al.* Coexistence of ferromagnetic and a re-entrant cluster glass state in the layered quaternary (Cr_{1-x}, M_nx_j2GeC. *Mater. Res. Lett.* **2**, 192–198 (2014).
13. Lin, S. *et al.* Magnetic and electrical/thermal transport properties of Mn-doped $M_{n+1}AX_n$ phase compounds $Cr_{2-x}Mn_xGaC$ ($0 \leq x \leq 1$). *J. Appl. Phys.* **113**, 053502 (2013).
14. Mockute, A. *et al.* Solid solubility and magnetism upon Mn incorporation in the bulk ternary carbides Cr_2AlC and Cr_2GaC. *Mater. Res. Lett.* **3**, 16–22 (2014).
15. Petruhins, A., Ingason, A. S., Lu, J., Magnus, F., Olafsson, S., Rosen, J. Synthesis and characterization of magnetic $(Cr_{0.5}Mn_{0.5})_2GaC$ thin films. *J Mater Sci* **50**, 4495–4502 (2015).
16. Salikhov, R., Semisalova, A. S., Petruhins, A., Ingason, A. S., Rosen, J., Wiedwald, U., *et al.* Magnetic Anisotropy in the $(Cr_{0.5}Mn_{0.5})_2GaC$ MAX Phase. *Mater Res Lett* **3**, 156–160 (2015).
17. Novoselova, I. P., Petruhins, A., Wiedwald, U., Weller, D., Rosen, J., Farle, M., *et al.* Long-term stability and thickness dependence of magnetism in thin $(Cr_{0.5}Mn_{0.5})_2GaC$ MAX phase films. *Mater Res Lett* **7**, 159–163 (2019).
18. Mockute, A. *et al.* Synthesis and ab initio calculations of nanolaminated (Cr, Mn_j2AlC compounds. *Phys. Rev. B* **87**, 094113 (2013).
19. Mockute, A. *et al.* Synthesis and characterization of arc deposited magnetic (Cr, Mn_j2AlC MAX phase films. *Phys. Status Solidi Rapid Res. Lett.* **8**, 420–423 (2014).
20. Meshkian, R., Ingason, A. S., Arnalds, U. B., Magnus, F., Lu, J., Rosen, J. A magnetic atomic laminate from thin film synthesis: $(Mo_{0.5}Mn_{0.5})_2GaC$. *APL Mater.* **3**, 076102 (2015).
21. Salikhov, R., Meshkian, R., Weller, D., Zingsem, B., Spoddig, D., Lu, J., *et al.* Magnetic properties of nanolaminated $(Mo_{0.5}Mn_{0.5})_2GaC$ MAX phase. *J. Appl. Phys.* **121**, 163904 (2017).
22. Tao, Q. *et al.* Thin film synthesis and characterization of a chemically ordered magnetic nanolaminate (V, Mn_j3Ga_C2. *APL Mater.* **4**, 086109 (2016).
23. Jaouen, M. *et al.* Invar like behavior of the Cr_2AlC MAX phase at low temperature. *J. Am. Ceram. Soc.* **96**, 3872–3876 (2013).
24. Jaouen, M. *et al.* Experimental evidence of Cr magnetic moments at low temperature in Cr_2A(A = Al, Ge)C. *J. Phys. Cond. Matter.* **26**, 176002 (2014).
25. Liu, Z. *et al.* Magnetic ground state of the $M_{n+1}AX_n$-phase nitride Cr_2GaN. *Phys. Rev. B* **88**, 134401 (2013).
26. Ingason, A. S. *et al.* A nanolaminated magnetic phase: Mn_2GaC. *Mater. Res. Lett.* **2**, 89–93 (2014).
27. Dahlqvist, M. *et al.* Magnetically driven anisotropic structural changes in the atomic laminate Mn_2GaC. *Phys. Rev. B* **93**, 014410 (2016).
28. Ingason, A. S., Pálsson, G. K., Dahlqvist, M. & Rosen, J. Long-range antiferromagnetic order in epitaxial Mn_2GaC thin films from neutron reflectometry. *Phys. Rev. B* **94**, 024416 (2016).
29. Novoselova, I. P. *et al.* Large uniaxial magnetostriction with sign inversion at the first order phase transition in the nanolaminated Mn_2GaC MAX phase. *Sci. Rep.* **8**, 2637 (2018).
30. Ingason, A. S., Dahlqvist, M. & Rosen, J. Magnetic MAX phases from theory and experiments; a review. *J. Phys. Cond. Matter* **28**, 433003 (2016).
31. Thore, A., Dahlqvist, M., Alling, B. & Rosen, J. Magnetic exchange interactions and critical temperature of the nanolaminate Mn_2GaC from first-principles supercell methods. *Phys. Rev. B* **93**, 054432 (2016).
32. Du, Y. L., Sun, Z. M., Hashimoto, H. & Barsoum, M. W. Electron correlation effects in the MAX phase Cr_2AlC from first-principles. *J. Appl. Phys.* **109**, 063707 (2011).
33. Ramzan, M., Lebègue, S. & Ahuja, R. Correlation effects in the electronic and structural properties of Cr_2AlC. *Phys. Status Solidi Rapid Res. Lett.* **5**, 122–124 (2011).
34. Ramzan, M., Lebègue, S. & Ahuja, R. Electronic and mechanical properties of Cr_2GeC with hybrid functional and correlation effects. *Solid State Commun.* **152**, 1147–1149 (2012).
35. Sun, W., Luo, W. & Ahuja, R. Role of correlation and relativistic effects in MAX phases. *J. Mater Sci.* **47**, 7615–7620 (2012).

36. Li, N., Dharmawardhana, C. C., Yao, K. L. & Ching, W.-Y. Theoretical characterization on intrinsic ferrimagnetic phase in nanoscale laminated Cr_2GeC. *Solid State Commun.* **174**, 43–45 (2013).
37. Mattesini, M. & Magnuson, M. Electronic correlation effects in the Cr_2GeC $M_{n+1}AX_n$ phase. *J. Phys. Cond. Matter* **25**, 035601 (2013).
38. Dahlqvist, M., Alling, B. & Rosen, J. Correlation between magnetic state and bulk modulus of Cr_2AlC. *J. Appl. Phys.* **113**, 216103 (2013).
39. Dahlqvist, M., Alling, B. & Rosen, J. A critical evaluation of GGA + *U* modeling for atomic, electronic and magnetic structure of Cr_2AlC, Cr_2GaC and Cr_2GeC. *J. Phys. Cond. Matter* **27**, 095601 (2015).
40. Hu, L., Wu, X. & Yang, J. Mn_2C monolayer: a 2D antiferromagnetic metal with high Néel temperature and large spin–orbit coupling. *Nanoscale* **8**, 12939–12945 (2016).
41. Dudarev, S. L., Botton, G. A., Savrasov, S. Y., Humphreys, C. J. & Sutton, A. P. Electron-energy-loss spectra and the structural stability of nickel oxide: An LSDA+U study. *Phys. Rev. B* **57**, 1505–1509 (1998).
42. Connolly, J. W. D. & Williams, A. R. Density-functional theory applied to phase transformations in transition-metal alloys. *Phys. Rev. B* **27**, 5169–5172 (1983).
43. Lindmaa, A., Lizárraga, R., Holmström, E., Abrikosov, I. A. & Alling, B. Exchange interactions in paramagnetic amorphous and disordered crystalline CrN-based systems. *Phys. Rev. B* **88**(054414), 054411–054415 (2013).
44. Blöchl, P. E. Projector augmented-wave method. *Phys. Rev. B* **50**, 17953–17979 (1994).
45. Kresse, G. & Joubert, D. From ultrasoft pseudopotentials to the projector augmented-wave method. *Phys. Rev. B* **59**, 1758–1775 (1999).
46. Kresse, G. & Hafner, J. Ab initio molecular dynamics for liquid metals. *Phys. Rev. B* **47**, 558–561 (1993).
47. Kresse, G. & Furthmüller, J. Efficiency of *ab-initio* total energy calculations for metals and semiconductors using a plane-wave basis set. *Comput. Mater Sci.* **6**, 15–50 (1996).
48. Kresse, G. & Furthmüller, J. Efficient iterative schemes for ab initio total-energy calculations using a plane-wave basis set. *Phys. Rev. B* **54**, 11169–11186 (1996).
49. Monkhorst, H. J. & Pack, J. D. Special points for Brillouin-zone integrations. *Phys. Rev. B* **13**, 5188–5192 (1976).
50. Perdew, J. P., Burke, K. & Ernzerhof, M. Generalized gradient approximation made simple. *Phys. Rev. Lett.* **77**, 3865–3868 (1996).
51. Perdew, J. P., Burke, K., Ernzerhof, M. Generalized gradient approximation made simple (Phys. Rev. Lett. 77, 3865, 1996). *Phys Rev Lett* **78**, 1396 (1997).
52. Perdew, J. P. *et al.* Restoring the density-gradient expansion for exchange in solids and surfaces. *Phys. Rev. Lett.* **100**, 136406 (2008).
53. Perdew, J. P. & Wang, Y. Accurate and simple analytic representation of the electron-gas correlation-energy. *Phys. Rev. B* **45**, 13244–13249 (1992).
54. Armiento, R. & Mattsson, A. E. Functional designed to include surface effects in self-consistent density functional theory. *Phys. Rev. B* **72**, 085108 (2005).
55. Mattsson, A. E. *et al.* The AM05 density functional applied to solids. *J. Chem. Phys.* **128**, 084714 (2008).
56. Mattsson, A. E. & Armiento, R. Implementing and testing the AM05 spin density functional. *Phys. Rev. B* **79**, 155101 (2009).
57. Perdew, J. P. & Zunger, A. Self-interaction correction to density-functional approximations for many-electron systems. *Phys Rev B* **23**, 5048–5079 (1981).
58. Hobbs, D., Kresse, G. & Hafner, J. Fully unconstrained noncollinear magnetism within the projector augmented-wave method. *Phys. Rev. B* **62**, 11556–11570 (2000).
59. Marsman, M. & Hafner, J. Broken symmetries in the crystalline and magnetic structures of γ-iron. *Phys. Rev. B* **66**, 224409 (2002).
60. Gyorffy, B. L., Pindor, A. J., Staunton, J., Stocks, G. M. & Winter, H. A first-principles theory of ferromagnetic phase-transitions in metals. *J. Phys. F Met. Phys.* **15**, 1337–1386 (1985).
61. Zunger, A., Wei, S. H., Ferreira, L. G. & Bernard, J. E. Special quasirandom structures. *Phys. Rev. Lett.* **65**, 353–356 (1990).
62. Alling, B., Marten, T. & Abrikosov, I. A. Effect of magnetic disorder and strong electron correlations on the thermodynamics of CrN. *Phys. Rev. B* **82**, 184430 (2010).

Acknowledgements

We acknowledge support from the Swedish Foundation for Strategic Research (SSF) for Project funding (EM16-0004) and from the Knut and Alice Wallenberg (KAW) Foundation for a Fellowship Grant and Project funding (KAW 2015.0043). The Swedish Research council is gratefully acknowledged through Project 642-2013-8020. The calculations were carried out using supercomputer resources provided by the Swedish National Infrastructure for Computing (SNIC) at the National Supercomputer Centre (NSC), the High Performance Computing Center North (HPC2N), and the PDC Center for High Performance Computing. Open access funding provided by Linköping University.

Author contributions

M.D. and J.R. conceived and designed the research and wrote the manuscript. M.D. performed all the calculations and analysed the calculated results together with J.R. All authors reviewed the manuscript.

Competing interests

The authors declare no competing interests.

Additional information

Supplementary information is available for this paper at https://doi.org/10.1038/s41598-020-68377-5.

Correspondence and requests for materials should be addressed to M.D. or J.R.

Reprints and permissions information is available at www.nature.com/reprints.

Publisher's note Springer Nature remains neutral with regard to jurisdictional claims in published maps and institutional affiliations.

Open Access This article is licensed under a Creative Commons Attribution 4.0 International License, which permits use, sharing, adaptation, distribution and reproduction in any medium or format, as long as you give appropriate credit to the original author(s) and the source, provide a link to the Creative Commons license, and indicate if changes were made. The images or other third party material in this article are included in the article's Creative Commons license, unless indicated otherwise in a credit line to the material. If material is not included in the article's Creative Commons license and your intended use is not permitted by statutory regulation or exceeds the permitted use, you will need to obtain permission directly from the copyright holder. To view a copy of this license, visit http://creativecommons.org/licenses/by/4.0/.

© The Author(s) 2020